A search for *B-L R*-parity-violating scalar top in $\sqrt{s}$ = 13 TeV *pp* collisions with the ATLAS experiment

The ATLAS Collaboration

A search is presented for the direct production of scalar top pairs which decay through an *R*-parity-violating coupling to a final state with two leptons and two jets, at least one of which is identified as a *b*-jet. The dataset consists of an integrated luminosity of 36.1 fb^{-1} of proton-proton collisions at a center-of-mass energy of $\sqrt{s}$ = 13 TeV, collected over 2015 and 2016 by the ATLAS detector at the LHC. No significant excess is observed over the Standard Model background, and exclusion limits are set on scalar top pair production at a 95% confidence level. Upper limits on the scalar top mass are set between 600 GeV and 1.5 TeV for branching fractions on the scalar top decay to an electron or muon and a *b*-quark above 10%.

1 Introduction

The extension of the Standard Model (SM) of particle physics with supersymmetry (SUSY) [1–6] leads to processes that violate both baryon number (B) and lepton number (L), leading to rapid proton decay and lepton-number-violating processes. A common theoretical approach to reconcile the strong constraints from the non-observation of these processes is to introduce a multiplicative quantum number called R-parity [7], defined as $R = (-1)^{3(B-L)+2s}$ where s is the spin of the particle. If R-parity is conserved, then SUSY particles are produced in pairs, and the lightest supersymmetric particle (LSP) is stable. The LSP cannot carry electric charge or color charge without coming into conflict with astrophysical data [8, 9].

A number of theoretical models beyond the Standard Model (BSM) predict R-parity violation [10–12]. The benchmark model of this search considers an additional local symmetry $U(1)_{B\text{-}L}$ to the $SU(3)_C \times SU(2)_L \times U(1)_Y$ Standard Model with right-handed neutrino supermultiplets. The minimal supersymmetric extension then only needs a vacuum expectation value for a right-handed scalar neutrino in order to spontaneously break the $B - L$ symmetry [13–17]. This minimal B-L model violates lepton number but not baryon number. The couplings for R-parity-violation (RPV) are highly suppressed, as they are related to the neutrino masses, and the model is consistent with the experimental bounds on proton decay and lepton number violation. At the LHC, the most noticeable effect is that the LSP is no longer stable and can now decay via R-parity-violating processes, and it also may now carry color and electric charge. This leads to unique signatures that are forbidden in conventional models with R-parity conservation. A novel possibility is a scalar top ($\tilde{t}$) LSP with a rapid RPV decay. Due to the large top quark mass, the lightest $\tilde{t}$ is expected to be significantly lighter than the other scalar quarks due to renormalization group effects [18, 19].

This document presents a search performed by ATLAS for direct scalar top pair production, with the RPV decay of each $\tilde{t}$ to a b-quark and a charged lepton ($\tilde{t} \rightarrow b\ell$), as shown in Figure 1. In contrast to R-parity conserving searches for $\tilde{t}$, there is no significant missing transverse momentum. The $\tilde{t}$ decay branching fractions to each lepton flavor may be different in a manner related to the neutrino mass hierarchy [20, 21]. For the inverted mass hierarchy, the branching fraction to electrons may be as large as 100%. For the normal mass hierarchy, the branching fraction to muons may be as high as 90%. Therefore, the experimental signature is two oppositely charged leptons of any flavor and two b-jets. For this analysis, only events with electron or muon signatures are selected, and final states are split by flavor into ee, $e\mu$, and $\mu\mu$ selections. At least one of the two jets is required to be identified as initiated by a b-quark, improving the selection efficiency of signal events over a two b-jet requirement. Events are chosen that reconstruct two $b\ell$ resonances of roughly equal mass.

Previous searches with similar final states have targeted the pair production of first, second, and third generation leptoquarks at ATLAS [22, 23] and at CMS [24]. However, they consider final states within the same generation ($eejj$, $\mu\mu jj$, $\tau\tau bb$ where j indicates a light flavor jet) and do not focus on final states with b-jets and electrons or muons ($eebb$, $\mu\mu bb$) nor consider final states with both electrons and muons ($e\mu bb$). The results of the Run 1 leptoquark searches were interpreted for the $\tilde{t}$ mass and its decay branching fractions in the $B - L$ model [20, 21], setting lower mass limits between 424 and 900 GeV at a 95% confidence level.

The ATLAS detector and the dataset collected during Run 2 of the LHC are described in Sec. 2, with the corresponding Monte Carlo simulation samples presented in Sec. 3. The identification and reconstruction of jets and leptons is presented in Sec. 4, and the discriminating variables used to construct the signal regions are described in Sec. 5. The method of background estimation is described in Sec. 6, and the
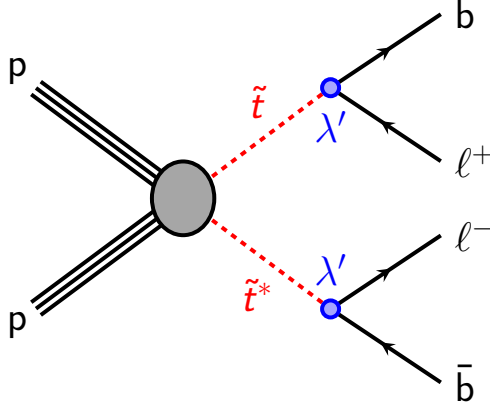
Figure 1: Feynman diagram for scalar top pair production, with $\tilde{t}$ and anti-$\tilde{t}$ ($\tilde{t}^*$) decay to a charged lepton and b-quark through an R-parity violating coupling λ'.

systematic uncertainties are detailed in Sec. 7. The results are presented in Sec. 8, and the conclusion given in Sec. 9.

2 ATLAS detector and data set

The ATLAS detector [25] consists of an inner detector tracking system, sampling electromagnetic and hadronic calorimeters, and a muon spectrometer. Charged-particle tracks are reconstructed in the inner detector (ID), which spans the pseudorapidity[1] range $|\eta| < 2.5$, and consists of three subdetectors: a silicon pixel tracker, a microstrip silicon tracker, and a straw-tube transition radiation tracker. The ID is surrounded by a thin solenoid providing an axial magnetic field of 2 T, allowing the measurement of charged-particle momenta. In preparation for Run 2, a new innermost layer of the silicon pixel tracker, the insertable B-layer (IBL) [26], was introduced at a radial distance of 3.3 cm from the beamline to improve track reconstruction and the identification of jets initiated by b-quarks.

The ATLAS calorimeter system consists of high-granularity electromagnetic and hadronic sampling calorimeters covering the region $|\eta| < 4.9$. The electromagnetic calorimeter uses liquid argon (LAr) as the active material with lead absorbers in the region $|\eta| < 3.2$. The central hadronic calorimeter incorporates plastic scintillator tiles and steel absorbers in the region $|\eta| < 1.7$. The hadronic endcap calorimeter ($1.5 < |\eta| < 3.2$) and forward calorimeters ($3.1 < |\eta| < 4.9$) also use LAr with copper or tungsten absorbers.

The muon spectrometer (MS) surrounds the calorimeters and measures muon tracks within $|\eta| < 2.7$ using three layers of precision tracking chambers and dedicated trigger chambers. A system of three superconducting air-core toroidal magnets provides a magnetic field for measuring muon momenta.

---

[1] ATLAS uses a right-handed coordinate system with its origin at the nominal interaction point (IP) in the center of the detector and the z-axis along the beam pipe. The x-axis points from the IP to the center of the LHC ring, and the y-axis points upward. Cylindrical coordinates (r, ϕ) are used in the transverse plane, ϕ being the azimuthal angle around the z-axis. The pseudorapidity is defined in terms of the polar angle θ as $\eta = -\ln\tan(\theta/2)$.

The ATLAS trigger system begins with a hardware-based Level 1 (L1) trigger followed by a software-based high-level trigger (HLT) [27]. The L1 trigger is designed to accept events at an average 100 kHz rate, and the HLT is designed to accept events that are written out to disk at an average rate of 1 kHz. Electrons are triggered in the pseudorapidity range $|\eta| < 2.5$, where the electromagnetic calorimeter is finely segmented and track reconstruction is available. Compact electromagnetic energy deposits triggered at L1 are used as the seeds for the HLT algorithms, which are designed to identify electrons based on calorimeter and fast track reconstruction. The muon trigger at L1 is based on a coincidence of trigger chamber layers. The parameters of muon candidate tracks are then derived in the HLT by fast reconstruction algorithms in both the ID and MS.

The data sample used for this search was collected from proton–proton collisions at a center-of-mass energy of $\sqrt{s}$ = 13 TeV in 2015 and 2016 while tracking detectors, calorimeters, muon chambers, and magnets were operating normally and corresponds to an integrated luminosity of 36.1 fb^{-1}. The uncertainty in the combined 2015+2016 integrated luminosity is 3.2%. It is derived, following a methodology similar to that detailed in Ref. [28], from a preliminary calibration of the luminosity scale using x-y beam-separation scans performed in August 2015 and May 2016. The LHC collided protons with bunch crossing intervals of 25 ns, and the average number of interactions per bunch crossing was estimated to be $\langle \mu \rangle$ = 23.7.

For this analysis, events are selected using single-electron and single-muon triggers requiring leptons above a transverse momentum (p_T) threshold and passing varying lepton identification and isolation criteria. The trigger-level criteria on the p_T, identification, and isolation of the leptons are looser than those applied in the event selection to ensure that trigger efficiencies are constant in the analysis phase space.

3 Monte Carlo simulation

Monte Carlo (MC) simulation is used to predict the backgrounds from SM processes, estimate the detector response and efficiency to reconstruct the signal process, and estimate systematic uncertainties. The largest sources of SM backgrounds are $t\bar{t}$, single-top, and Z+jets production, and their yields are estimated through data-driven methods described in Sec. 6. The smaller backgrounds are W+jets, diboson, and $t\bar{t}$ +W/Z production and are estimated directly from MC simulation. The contribution from backgrounds with jets misreconstructed as leptons or with non-prompt leptons is negligible, and is therefore determined from MC simulation. Details of the MC simulations are given below and are summarized in Table 1.

Process	Event generator	PS and hadronization	UE tune	PDF	Cross-section
$t\bar{t}$	Powheg-Box v2	Pythia 6.428	P2012	CT10	NNLO+NNLL [29]
single-top					
(Wt and s-channel)	Powheg-Box v2	Pythia 6.428	P2012	CT10	NNLO+NNLL [30, 31]
(t-channel)	Powheg-Box v1	Pythia 6.428	P2012	CT10	NNLO+NNLL [32]
Z/W+jets	Sherpa 2.2.1	Sherpa 2.2.1	Default	NNPDF3.0	NNLO [33]
Diboson	Sherpa 2.2.1	Sherpa 2.2.1	Default	NNPDF3.0	NLO
Diboson (add. rad.)	Sherpa 2.1.1	Sherpa 2.1.1	Default	CT10	NLO
$t\bar{t}$ +W/Z	MG5_aMC@NLO 2.2.3	Pythia 8.212	A14	NNPDF2.3	NLO
$\tilde{t}\tilde{t}^*$	MG5_aMC@NLO 2.2.3	Pythia 8.186	A14	NNPDF2.3	NLO+NLL [34]

Table 1: MC simulation details by physics process.

The $t\bar{t}$ and single-top processes [35] are simulated at next-to-leading order (NLO) accuracy in perturbative QCD using the Powheg-Box [36] v2 generator for $t\bar{t}$, Wt, and s-channel single-top production, and using the Powheg-Box v1 generator for the electroweak t-channel single-top production. For these processes the top spin correlations are preserved, and the top quark mass is set to 172.5 GeV. The matrix element is interfaced with the CT10 [37] parton distribution function (PDF) set, with the parton shower (PS), fragmentation, and underlying event are simulated with Pythia 6.428 [38] using the CTEQ6L1 [39] PDF set and P2012 [40] underlying event tuned parameters (UE tune), with additional radiation simulated to the leading-logarithmic approximation through p_T-ordered parton showers [41].

The Z+jets and W+jets samples [42] are generated at NLO with the Sherpa 2.2.1 [43] generator. Matrix elements are calculated for up to 2 partons at NLO and 4 partons at LO using the Comix [44] and OpenLoops [45] matrix element generators and merged with the Sherpa PS [46] using the ME+PS@NLO prescription [47]. The NNPDF3.0 [48] PDF set is used in conjunction with dedicated PS tuning developed by the Sherpa authors. Diboson samples with two, three, or four leptons are similarly generated with Sherpa 2.2.1. The diboson matrix elements contain all diagrams with four electroweak verticies, and are calculated for up to one (ZZ) or zero (WW,WZ) partons at NLO and up to three partons at LO. Diboson events produced in association with additional radiation are simulated with Sherpa 2.1.1, using the same prescriptions as above but with the CT10 PDF set used in conjunction with the dedicated Sherpa PS tuning. The production of $t\bar{t}$ pairs in assocation with W and Z bosons ($t\bar{t} + V$) is generated at NLO using MadGraph5_aMC@NLO (MG5_aMC@NLO) 2.2.3 [49] and interfaced to Pythia 8.212 [50] with the CKKW-L [51] prescription. It uses the A14 [52] UE tune and NNPDF2.3 [53] PDF set.

The RPV scalar top signal events are generated at leading-order using the MG5_aMC@NLO 2.2.3 generator with the NNPDF2.3 PDF set and interfaced to Pythia 8.186 [50] using the A14 UE tune. The matrix element is matched to the PS using the CKKW-L prescription, with the matching scale set to one quarrter of the generated scalar top mass. All other supersymmetric particles are assumed to be decoupled. The signal cross sections are calculated to NLO accuracy in the strong coupling constant, adding the resummation of soft gluon emission at next-to-leading-logarithmic accuracy (NLO+NLL) [54–57]. The nominal cross section and the uncertainty for each mass point are taken from a combination of cross section predictions using different PDF sets and factorization and renormalization scales, as described in Ref. [34]. Scalar top samples are generated at masses between 600 and 1000 GeV in steps of 100 GeV and between 1000 and 1600 GeV in steps of 50 GeV. The cross section ranges from 175 ± 23 fb for a $\tilde{t}$ mass of 600 GeV to 0.141 ± 0.038 fb for a mass of 1600 GeV. The generated scalar tops decay promptly through $\tilde{t} \rightarrow b\ell$ with a 1/3 branching ratio (Br) into each lepton flavour. When optimizing the signal event selection, the generated events are reweighted to have $Br(\tilde{t} \rightarrow be) = Br(\tilde{t} \rightarrow b\mu) = 0.5$ and $Br(\tilde{t} \rightarrow b\tau) = 0$, and various weightings are used to derive limits for different branching ratio assumptions.

All background samples are normalized to the available NLO or NNLO cross sections, as indicated in Table 1. The modeling of c-hadron and b-hadron decays in samples generated with Powheg-Box or MG5_aMC@NLO is performed with EvtGen 1.2.0 [58]. Generated events are propagated through a full simulation [59] of the ATLAS detector based on Geant4 [60] which describes the interactions of the particles with the detector. A parameterized simulation of the ATLAS calorimeter called Atlfast-II [59] is used for faster detector simulation of signal samples, and is found to have good agreement with the full simulation. Multiple overlapping pp interactions (pileup) are included in by overlaying simulated minimum bias events onto the simulated hard scatter event. Minimum bias events are generated using Pythia 8.186 with the A2 [61] UE tune and MSTW2008LO [62] PDF set. The simulated events are

weighted such that the distribution of the average number of pp interactions per bunch crossing agrees with data.

4 Event reconstruction

Events, leptons, and jets are required to pass several quality criteria to be considered by the analysis. Events recorded during stable beam and detector conditions are required to pass data-quality criteria [63]. Each event is required to have a primary reconstructed vertex with two or more associated tracks with $p_T > 400$ MeV, where the primary vertex is chosen as the vertex with the highest Σp_T^2 of associated tracks. Two stages of quality and kinematic requirements are applied to leptons and jets. The looser baseline requirements are first applied, and baseline leptons and jets are used to resolve any misidentification or overlap between electrons, muons, and jets. The subsequent tighter signal requirements are then applied to identify high-quality leptons and jets in the kinematic phase-space of interest.

Electron candidates are reconstructed from energy deposits in the electromagnetic calorimeter matched to a charged particle track in the ID. Baseline electron candidates must have $p_T > 10$ GeV, $|\eta| < 2.47$, and satisfy a loose electron likelihood identification [64]. Signal electrons must pass the baseline electron selection, have $p_T > 40$ GeV, and satisfy a tight electron likelihood identification. In addition they must be isolated from nearby activity, passing a loose p_T-dependent track-based criterion [65]. Finally, their trajectory must be consistent with the primary vertex, such that their impact parameter in the transverse plane (d_0^{PV}) satisfies $|d_0^{PV}|/\sigma_{d_0^{PV}} < 5$, where $\sigma_{d_0^{PV}}$ is the uncertainty on d_0^{PV}. The distance between the impact parameter and the primary vertex along the beam direction (z_0^{PV}) must also satisfy $|z_0^{PV} \sin\theta| < 0.5$ mm.

Muon candidates are reconstructed by combining tracks in the ID and track segments in the MS. Baseline muon candidates must have $p_T > 10$ GeV, $|\eta| < 2.7$, and satisfy the medium muon identification criteria [66]. Signal muons must pass the baseline muon selection, have $p_T > 40$ GeV, $|\eta| < 2.5$, $|z_0^{PV} \sin\theta| < 0.5$ mm, and $|d_0^{PV}|/\sigma_{d_0^{PV}} < 3$. As with electrons, muons must pass the p_T-dependent loose track-based isolation criteria. Events containing a poorly measured signal muon, as determined by having incompatible momentum measurements in the ID and the MS, are rejected. Absolute requirements on the impact parameter of signal muons are also applied to reject cosmic muons, requiring $|z_0^{PV}| < 1$ mm and $|d_0^{PV}| < 0.2$ mm.

Jets are reconstructed using the anti-k_t algorithm [67, 68] with a radius parameter $R = 0.4$ from clusters of energy deposits in the calorimeters [69]. Jets are corrected for pileup contamination on a per-event basis using the jet area subtraction method [70, 71]. Jets are further calibrated to account for the predicted detector response in MC simulation, and a residual calibration of jets in data is derived through *in situ* measurements [72]. Baseline jet candidates are required to have $p_T > 20$ GeV and $|\eta| < 2.8$. Jets with $p_T < 60$ GeV and $|\eta| < 2.4$ are required to pass pileup-rejection criteria implemented via the jet vertex tagger (JVT) algorithm [70]. Signal jets must pass the baseline jet selection and have $p_T > 60$ GeV. Events with jets that fail the loose quality criteria [73] to identify noise bursts and non-collision backgrounds are rejected. Jets initiated by b-quarks are identified using the multivariate MV2c10 b-tagging algorithm [74, 75], which exploits the impact parameters of charged particle tracks, the parameters of reconstructed secondary vertices, and the topology of b- and c-hadron decays inside a jet. The working point is chosen to provide a b-tagging efficiency of 77% per b-jet in simulated $t\bar{t}$ events with a rejection factor of approximately 130 for light quark- and gluon-initiated jets and 6 for c-quark-initiated jets [75]. Correction

factors are applied to events to compensate for differences between data and MC simulation in the b-tagging efficiency for b-, c-, and light-jets.

To avoid reconstructing a single detector signature as multiple leptons or jets, an overlap removal procedure is performed on baseline leptons and jets. The requirements are applied sequentially, and failing particles are removed from consideration in the subsequent steps. If an electron and muon share a track in the ID, the electron is removed. Any jet that is not b-tagged and is within a distance[2] $\Delta R(\ell, \text{jet}) \leq 0.20$ of a lepton is removed. If the jet is b-tagged, the lepton is removed instead in order to suppress leptons from semi-leptonic decays of c- and b-hadrons. Finally, any lepton within $\Delta R(\ell, \text{jet}) \leq 0.40$ of a jet is removed.

The identification, reconstruction, isolation, and trigger efficiencies of electrons [65] and muons [66] in MC simulation are corrected using events in data with leptonic Z and J/ψ decays. Similarly, corrections to the b-tagging efficiency and mis-tag rate in MC simulation are derived from various control regions in data [75].

5 Event selection

To identify the pair production of scalar tops, events are required to have at least two leptons and two jets. If more than two leptons or two jets are found, the objects with the highest p_{T} are selected. At least one of the two leading jets must be b-tagged. The selected leptons are required to have opposite charge, and one of them must be consistent with the associated single-lepton trigger. This trigger requirement is highly efficient for signal events, with an efficiency of 93% for the $\mu\mu$ channel and 98% for the ee channel.

The lepton–jet pair of each $\tilde{t}$ decay will roughly reconstruct the invariant mass $m_{b\ell}$ of the original $\tilde{t}$. In an event with two leptons and two jets, two pairings are possible; one that reconstructs the correct $\tilde{t}$ masses, and one which inverts the pairing and incorrectly reconstructs the masses. As the two masses should be roughly equal, the pairing which minimizes the mass asymmetry between $m_{b\ell}^0$ and $m_{b\ell}^1$ is chosen, defined as

$$m_{b\ell}^{\mathrm{asym}} = \frac{m_{b\ell}^0 - m_{b\ell}^1}{m_{b\ell}^0 + m_{b\ell}^1}.$$

Here $m_{b\ell}^0$ is chosen to be the larger of the two masses. Events are further selected to have small mass asymmetry $m_{b\ell}^{\mathrm{asym}} < 0.2$. This reduces the contamination from background processes, whose random pairings lead to a more uniform $m_{b\ell}^{\mathrm{asym}}$ distributions.

Two nested signal regions (SRs) are constructed to optimize the identification of signal over background events. The signal regions are optimized using MC signal and background predictions, assuming $\tilde{t}$ decays of $Br(\tilde{t} \to be) = Br(\tilde{t} \to b\mu) = 50\%$. A primary kinematic selection of the signal regions is on $m_{b\ell}^0$, with SR800 requiring $m_{b\ell}^0 > 800$ GeV and SR1100 requiring $m_{b\ell}^0 > 1100$ GeV. By defining two signal regions the sensitivity to high mass signals above 1.1 TeV is improved, while still allowing for sensitivity to lower mass signals. Several other kinematic selections, common to both SRs, are defined to reduce the

---

[2] The distance between two four-vectors is defined as $\Delta R = \sqrt{(\Delta\eta)^2 + (\Delta\phi)^2}$, where $\Delta\eta$ is their distance in pseudorapidity and $\Delta\phi$ is their azimuthal distance. The distance with respect to a jet is calculated from its central axis.

contribution of the largest backgrounds. As the $\tilde{t}$ decay products are generally very energetic, a selection on their p_T sum,

$$H_T = \sum_{i=1}^{2} p_T^{\ell_i} + \sum_{j=1}^{2} p_T^{\text{jet}_j}$$

is applied, such that $H_T > 1000$ GeV. To reduce contamination from Z+jets events, a requirement is placed on the invariant mass of two same-flavor leptons, with $m_{\ell\ell} > 300$ GeV. A large fraction of background processes involving a top quark is suppressed through the requirement on $m_{b\ell}^0$ and $m_{b\ell}^{\text{asym}}$, with correctly reconstructed top masses falling well below the signal region requirements. However, top decays in which the lepton and b-jet decay products are mispaired can enter the SRs if the incorrectly reconstructed masses are large. In such cases it is the rejected pairing that properly reconstructs the top decay, with one of the two $b\ell$ pair masses below the kinematic limit for a top decay. To suppress such backgrounds, events are rejected if the subleading $b\ell$ mass of the rejected pairing, $m_{b\ell}^1(\text{rej})$, is compatible with that of a reconstructed top quark, with $m_{b\ell}^1(\text{rej}) < 150$ GeV.

The distribution of predicted signal and background events is shown for the SR800 region in Fig. 2 for $m_{b\ell}^0$, H_T, $m_{b\ell}^{\text{asym}}$, $m_{\ell\ell}$, and $m_{b\ell}^1(\text{rej})$, demonstrating the potential for background rejection. For the 1 TeV (1.5 TeV) mass signal model, the SR800 selections are 21% (24%) efficient for events with two $\tilde{t} \rightarrow be$ decays, 16% (16%) for events with two $\tilde{t} \rightarrow b\mu$ decays, and 0.1% (0.3%) for events with two $\tilde{t} \rightarrow b\tau$ decays.

6 Background estimation

For each of the relevant backgrounds in the signal regions, one of two methods is used to estimate the contribution. For the minor diboson, $t\bar{t} + V$, and W+jets backgrounds, the prediction from MC simulation is taken, corrected to the highest order theoretical cross section available. For the dominant $t\bar{t}$, single-top, and Z+jets backgrounds, the expected yield in the SRs is estimated by scaling each MC prediction by a normalization factor (NF) derived from three dedicated control regions (CRs), one for each background process. Each control region is defined to be kinematically close to the SRs while inverting or relaxing specific selections to enhance the contribution of the targeted background process while reducing the contamination from other backgrounds and the benchmark signals.

To derive a background-only estimation, the normalizations of the $t\bar{t}$, single-top, and Z+jets backgrounds are determined through a likelihood fit [76] performed simultaneously to the observed number of events in each CR. The expected yield in each region is given by the sum over all background processes in the ee, $e\mu$, and $\mu\mu$ channels inclusively. The NF for each of the $t\bar{t}$, single-top, and Z+jets backgrounds are free parameters of the fit. The systematic uncertainties are treated as nuisance parameters in the fit.

Several validation regions (VRs) are defined to test the extrapolation from the CRs to SRs over the relevant kinematic variables. The VRs are disjoint from both the CRs and SRs, and are constructed to fall between one or more CRs and the SRs in one of the extrapolated variables. The VRs are not included in the fit, but provide a statistically independent cross-check of the background prediction in regions with a negligible signal contamination. Three VRs are constructed to test the extrapolation in the $m_{b\ell}^0$, $m_{b\ell}^1(\text{rej})$, and H_T observables. A fourth VR is constructed to validate the extrapolation of the Z+jets CR in $m_{\ell\ell}$. Details of
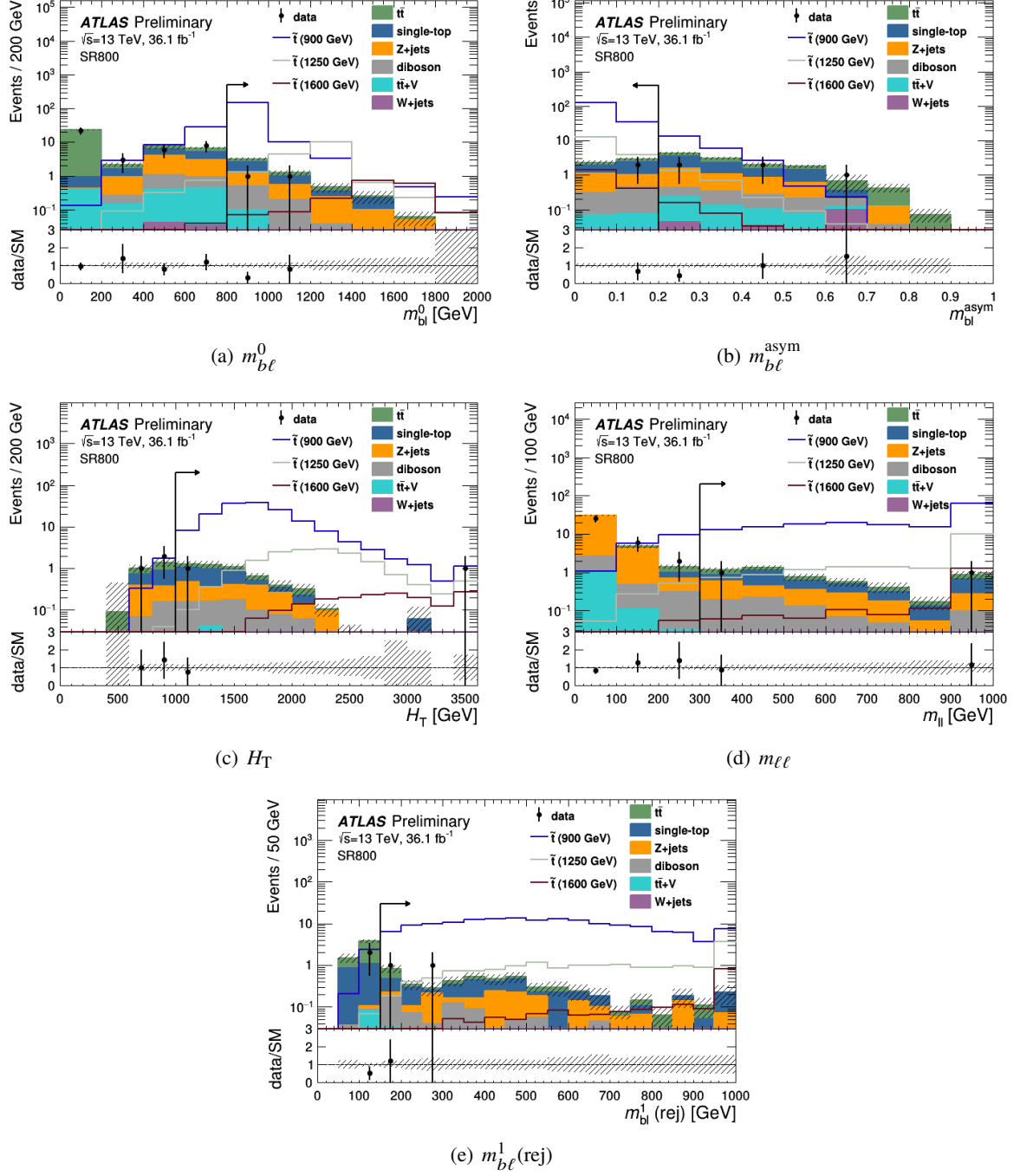
(a) $m_{b\ell}^0$

(b) $m_{b\ell}^{\mathrm{asym}}$

(c) H_{T}

(d) $m_{\ell\ell}$

(e) $m_{b\ell}^1(\mathrm{rej})$

Figure 2: A comparison of data to the post-fit MC prediction in $m_{b\ell}^0$ (a), $m_{b\ell}^{\mathrm{asym}}$ (b), H_{T} (c), $m_{\ell\ell}$ (d), and $m_{b\ell}^1(\mathrm{rej})$ (e) in the SR800 signal region. The SR800 event selections are applied for each distribution except the selection on the variable shown, which is indicated by an arrow. Normalization factors are derived from the background-only estimation discussed in Sec. 6 and are applied to the dominant $t\bar{t}$, single-top, and Z+jets processes. Benchmark signal models generated at masses of 900, 1250, and 1600 GeV are included for comparison. The bottom panel shows the ratio between the data and SM prediction. The hashed uncertainty band includes the statistical uncertainties on the background prediction. The last bin includes the overflow events.

9

the selection criteria in each CR and VR are presented below, and a summary of the selections is provided in Table 2.

Region	N_b	$m_{b\ell}^0$ [GeV]	$m_{b\ell}^1$(rej)[GeV]	H_T [GeV]	$m_{\ell\ell}$ [GeV]	m_{CT} [GeV]
SR800	≥ 1	> 800	> 150	> 1000	> 300	–
SR1100	≥ 1	> 1100	> 150	> 1000	> 300	–
CRtt	≥ 1	[200,500]	< 150	[600,800]	> 300	$< 200^*$
CRst	$= 2$	[200,500]	< 150	< 800	> 120	> 200
CRZ	≥ 1	> 700	–	> 1000	[76.2,106.2]	–
VR$m_{b\ell}^0$	≥ 1	> 500	< 150	[600,800]	> 300	–
VR$m_{b\ell}^1$(rej)	≥ 1	[200,500]	> 150	[600,800]	> 300	–
VRH_T	≥ 1	[200,500]	< 150	> 800	> 300	–
VRZ	$= 0$	[500,800]	> 150	> 1000	> 300	–

Table 2: Summary of the selections of the signal, control, and validation regions. All regions require at least two oppositely charged leptons and at least two jets. Each region requires at least one of the two leading jets to be b-tagged with the exception of CRst, which requires both leading jets to be b-tagged, and VRZ, which requires zero b-tagged jets in the event. A mass asymmetry selection of $m_{b\ell}^{\text{asym}} < 0.2$ is applied to all regions. The contransverse mass selection m_{CT} (Eq. 1) is only applied to events in CRtt with exactly two b-tagged jets, as indicated by the *, ensuring the region is orthogonal to CRst.

6.1 Single-top control region

The single-top background enters the SR through the Wt process, when the $b\ell$ pair produced in the leptonic top quark decay are incorrectly paired with the lepton from the W decay and an additional jet from QCD radiation. The CRst control region is designed to target the Wt production in a less-energetic kinematic region or where the rejected $b\ell$ pairing correctly associates the decay products of the top quark. To separate CRst from the SRs, the H_T and $m_{b\ell}^0$ requirements are reversed such that $H_T < 800$ GeV and $200 < m_{b\ell}^0 < 500$ GeV. To target events in which the top quark is reconstructed in the rejected $b\ell$ pairing, the selection on $m_{b\ell}^1$(rej) is reversed, requiring $m_{b\ell}^1$(rej) < 150 GeV. As there is no dilepton resonance in this background process the $m_{\ell\ell}$ selection is reduced to increase the CRst yield and improve the statistical precision of the constraint.

The cross section of the Wt process is significantly lower than that of $t\bar{t}$ production. The contransverse mass (m_{CT}) [77] is introduced to discriminate between Wt and $t\bar{t}$ events and increase the Wt purity in the CRst. The m_{CT} observable attempts to reconstruct the invariant mass of pair-produced, semi-invisibly decaying heavy particles. For two identical decays of top quarks into two visible b-quarks b_1 and b_2, and two W bosons, each of whose decay products may include an invisible particle, m_{CT} is defined as

$$m_{CT}^2(b_1, b_2) = [E_T(b_1) + E_T(b_2)]^2 - [\mathbf{p}_T(b_1) - \mathbf{p}_T(b_2)]^2, \tag{1}$$

where $E_T = \sqrt{p_T^2 + m^2}$. For an event with two top quarks, the m_{CT} observable will therefore have a kinematic endpoint at

$$m_{CT}^{\text{max}} = \frac{m_t^2 - m_W^2}{m_t},$$

where m_t and m_W are the masses of the top quark and W boson, respectively. A lower cut on this variable is effective at suppressing the $t\bar{t}$ background, for which m_{CT} has a kinematic endpoint of about 135 GeV,

and a strict requirement of $m_{CT} > 200$ GeV is applied in CRst. The m_{CT} variable is only effective at rejecting $t\bar{t}$ events in which the b-quark decay products of both top quarks are properly identified, and both leading jets (and only the leading jets) are required to be b-tagged in CRst, such that $N_b = 2$. The m_{CT} distribution of the backgrounds in CRst is shown in Fig. 3(a) when no m_{CT} requirement is applied, and a significant single-top contribution is seen for $m_{CT} > 200$ GeV.

6.2 $t\bar{t}$ control region

The CRtt control region is constructed to target $t\bar{t}$ events with kinematics similar to the SRs. As with CRst, the H_T and $m_{b\ell}^0$ requirements are inverted such that $600 < H_T < 800$ GeV and $200 < m_{b\ell}^0 < 500$ GeV. The selection on $m_{b\ell}^1(\text{rej})$ is also inverted, requiring $m_{b\ell}^1(\text{rej}) < 150$ GeV, such that one of the two top quarks is reconstructed in the rejected $b\ell$ pairings. The distribution of $m_{b\ell}^1(\text{rej})$ in CRtt is shown in Fig. 3(b), showing the mispairing of $t\bar{t}$ events is well-modeled in MC simulation. Due to the larger cross section of the $t\bar{t}$ process, contamination from Wt events is minimal. However, to maintain orthogonality with CRst, a requirement of $m_{CT} < 200$ GeV is applied to events in which both leading jets (and only the leading jets) are b-tagged, with $N_b = 2$.

6.3 Z+jets control region

The CRZ control region targets Z+jets events by applying a selection on the invariant mass of the dilepton pair $m_{\ell\ell}$, requiring it to be within 15 GeV of the Z mass. Both leptons are required to be of the same flavor. The $m_{\ell\ell}$ selection is effective at removing signal contamination, and the SR H_T selection is left unchanged, while the $m_{b\ell}^0$ selection is slightly relaxed to $m_{b\ell}^0 > 700$ GeV to enchance the event yield.

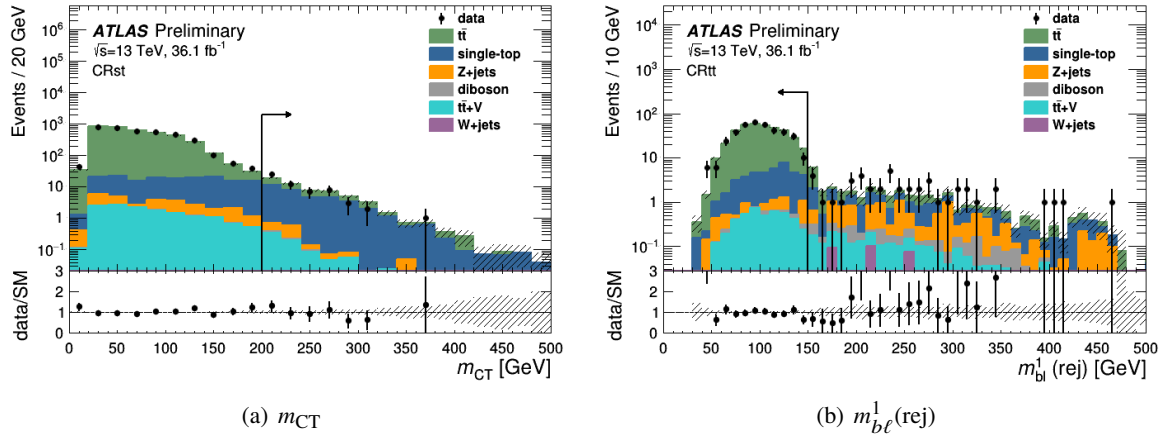(a) m_{CT} (b) $m_{b\ell}^1(\text{rej})$

Figure 3: A comparison of data to the post-fit MC prediction for (a) m_{CT} in CRst and (b) $m_{b\ell}^1(\text{rej})$ in CRtt. The relevant CR event selections are applied for each distribution except the selection on the variable shown, which is indicated by an arrow. Normalization factors are derived from the background-only fit configuration and are applied to the dominant $t\bar{t}$, single-top, and Z+jets processes. The bottom panel shows the ratio between the data and SM prediction. The hashed uncertainty band includes the statistical uncertainties on the background prediction. The last bin includes the overflow events.

6.4 Validation regions

Four disjoint validation regions are developed to test the extrapolation of the background fit between the CRs and SRs. A full list of the region selections is given in Table 2. The $VRm_{b\ell}^0$, $VRm_{b\ell}^1(\text{rej})$, and VRH_T test the extrapolation from CRst and CRtt to the SRs in the $m_{b\ell}^0$, $m_{b\ell}^1(\text{rej})$, and H_T observables by requiring $m_{b\ell}^0 > 500$ GeV, $m_{b\ell}^1(\text{rej}) > 150$ GeV, and $H_T > 800$ GeV, respectively. In this way $VRm_{b\ell}^0$, $VRm_{b\ell}^1(\text{rej})$, and VRH_T all lie between the SRs and both CRtt and CRst, with signal contamination below 1% for all signal mass points. No requirement is placed on m_{CT} in any VR, allowing both $t\bar{t}$ and Wt contributions to be validated.

A fourth validation region, VRZ, is developed to extrapolate between CRZ and the SRs in the $m_{\ell\ell}$ observable, requiring $m_{\ell\ell} > 300$ GeV. As the $m_{\ell\ell}$ variable provides the only separation between CRZ and the SRs, the requirement on $m_{b\ell}^0$ is relaxed to $500 < m_{b\ell}^0 < 800$ GeV, and any event with a b-tagged jet is rejected, such that $N_b = 0$. The Z+jets MC prediction models the data well in both $m_{b\ell}$ and N_b, with a signal contamination in VRZ below 5% for mass points above 1 TeV.

The observed data yield and the post-fit background prediction for each CR and VR are shown in Fig. 4. Good agreement is seen in all validation regions, with differences between the data and SM prediction below 1σ. The modeling of the extrapolated variable for each VR is shown in Fig. 5, demonstrating good agreement in the shape of the variables of interest.
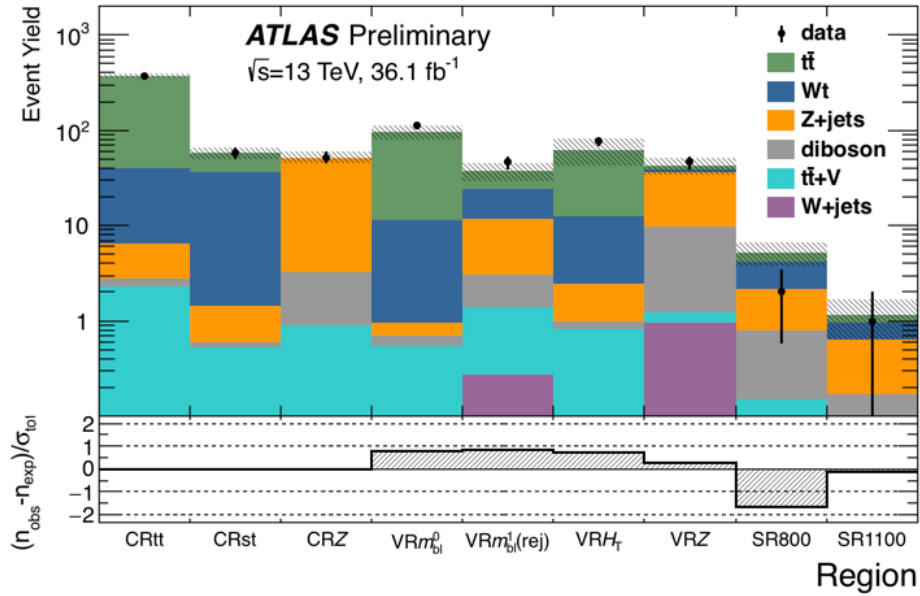

Figure 4: Comparison of the observed data and expected number of events in the CRs, VRs, and SRs. The background prediction is derived with the background-only fit configuration, and the hashed band includes the total uncertainty on the background prediction. The bottom panel shows the significance of the difference between data and the background prediction.
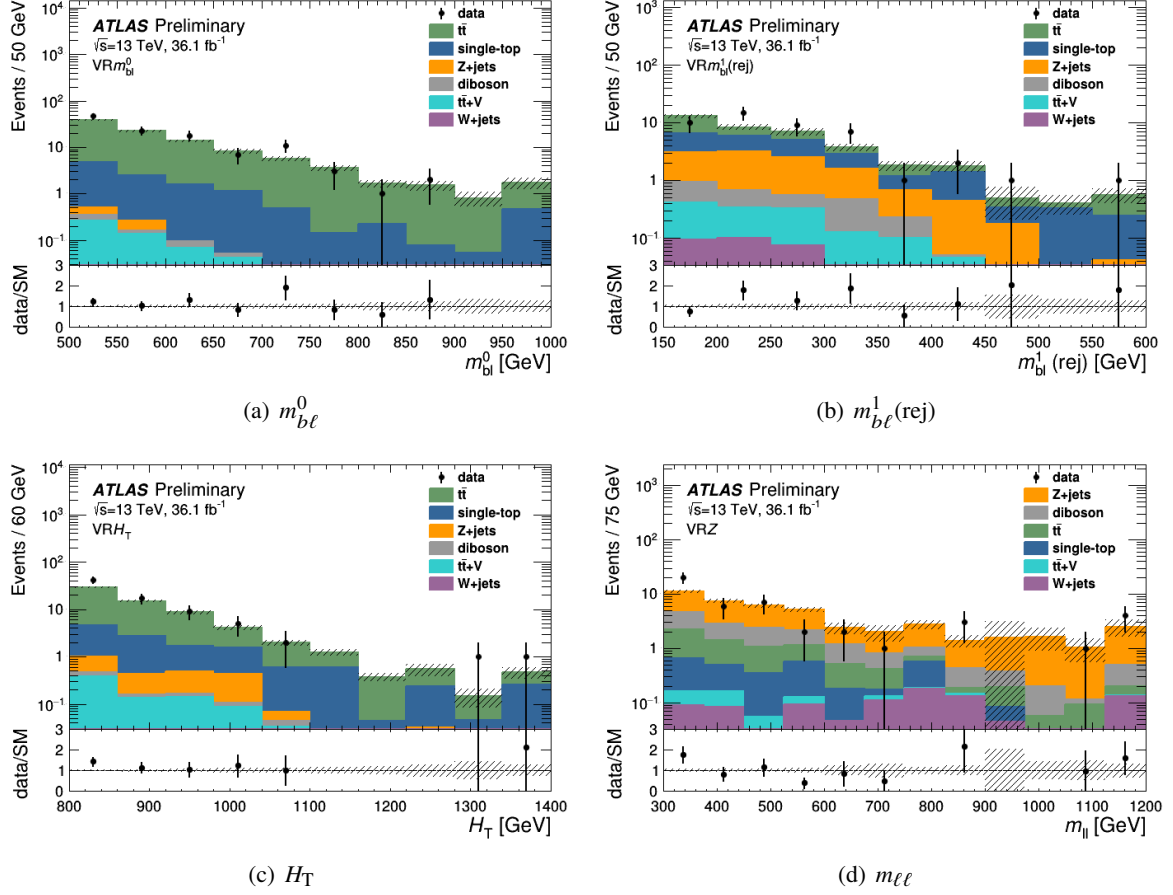
Figure 5: A comparison of data to the post-fit MC prediction for (a) $m_{b\ell}^0$ in VR$m_{b\ell}^0$, (b) $m_{b\ell}^1$(rej) in VR$m_{b\ell}^1$(rej), (c) H_T in VRH_T, and (d) $m_{\ell\ell}$ in VRZ. Normalization factors are derived from the background-only fit configuration and are applied to the dominant $t\bar{t}$, single-top, and Z+jets processes. The bottom panel shows the ratio between the data and SM prediction. The hashed uncertainty band includes the statistical uncertainties on the background prediction. The last bin includes the overflow events.

7 Systematic uncertainties

Systematic uncertainties on the signal and background predictions arise from theoretical sources on the expected yield and MC modeling, and from experimental sources.

Experimental uncertainties reflect the precision of the energy and momentum calibration of jets and leptons, as well as the assumptions on the identification and reconstruction efficiencies in MC simulation. The dominant experimental uncertainties are related to jets, including those in the jet energy scale and resolution [72, 78] and the calibration of the b-tagging efficiency for b-, c-, and light-flavor jets [75]. The largest experimental uncertainties on the fitted background prediction in SR800 (SR1100) are in jet energy resolution at 2% (10%) and the b-tagging efficiency of light-flavor jets at 2% (4%). The experimental uncertainties on leptons each have a small impact on the final measurement, which includes uncertainties in the energy scale and resolution of electrons [65] and muons [66], and the calibration of the lepton trigger, identification, reconstruction, and isolation efficiencies. The 3.2% uncertainty on the measured integrated luminosity also has a marginal effect on the final result.

Uncertainties on the MC modeling of the $t\bar{t}$ and Wt backgrounds account for the choice of MC generator, variations in the hadronization and fragmentation processes, and the amount of initial- and final-state radiation [35]. As the $t\bar{t}$ (Wt) background normalization is constrained in the likelihood fits, the uncertainty on the transfer of the NF from the CRtt (CRst) to both SR800 and SR1100 is derived by comparing signal-to-control region yields in alternative models. The uncertainty on the background estimation due to the choice of MC generator is derived for $t\bar{t}$ and Wt by comparing the SR-to-CR NF derived using MG5_AMC@NLO 2.2.3 against POWHEG-BOX v2, both showered with HERWIG++ v2.7.1 [79] using the UEEE5 [80] UE tune. The hadronization and fragmentation modeling is similarly evaluated in both $t\bar{t}$ and Wt by comparing the nominal POWHEG+PYTHIA sample with the same POWHEG+HERWIG sample. The uncertainty related to initial and final state radiation is evaluated for both $t\bar{t}$ and Wt by varying the parameters of the generator and P2012 UE tune in the nominal POWHEG+PYTHIA sample related to NLO radiation and the factorization and renormalization scale. An uncertainty on the single-top yield due to the destructive interference between the $t\bar{t}$ and Wt processes is measured using inclusively-generated $WWbb$ events at LO, and compared with the combined yields of LO-generated $t\bar{t}$ and Wt samples. The uncertainty on the total background estimate is found to be 8-45% from $t\bar{t}$ samples and 22% from single-top samples.

The theoretical uncertainties on the Z+jets, diboson, and $t\bar{t}+V$ samples are calculated by varying generator parameters related to the factorization, renormalization, resummation, and CKKW matching scales. The envelope of these variations is taken as the theoretical uncertainty on the predicted yield in each SR, with total uncertainties on the background estimation of 2-4% for Z+jets, 4% for diboson, and $\sim 1\%$ for $t\bar{t} + V$ samples. As the diboson and $t\bar{t} + V$ samples are not normalized in the CRs, the uncertainty on the theoretical cross section is also included. The uncertainty on the NLO cross section is found to be 6% for the diboson process [81] and 13% for the $t\bar{t} + V$ process [49]. A 50% uncertainty is applied to the small W+jets yield in both SRs.

The cross section uncertainties on the scalar top signal models are derived from the envelope of cross section predictions from several distinct PDF sets and varying the factorization and renormalization scales, as described in Ref. [34]. The uncertainty on the cross section varies from 13% for the 600 GeV mass point to 27% for the 1.6 TeV mass point.

8 Results

The observed yield and fitted background prediction in SR800 and SR1100 are shown in Table 3. One event is observed in SR1100 and two are observed in SR800, in agreement with the SM prediction. The SR1100 event is included in SR800 by definition, and both events are found in the $\mu\mu$ channel. The observed and predicted $m_{b\ell}^0$, H_{T}, $m_{b\ell}^{\mathrm{asym}}$, $m_{\ell\ell}$, and $m_{b\ell}^1$(rej) distributions in SR800 are shown in Fig. 2.

For each SR, model-independent upper limits are derived on the cross section of potential BSM processes at a 95% confidence level (CL). A likelihood fit is performed to the number of observed events in all three CRs and the target SR, and a generic signal model is assumed to contribute to the SR only. No theoretical or systematic uncertainties are considered for the signal model except the luminosity uncertainty. The observed and expected limits on the number of BSM events, as well as the observed limit on the visible cross section, are shown in the lower rows of Table 3.

Exclusion limits are derived at 95% CL for the $\tilde{t}$ signal samples. Limits are obtained through a profile log-likelihood ratio test using the CL$_{\mathrm{S}}$ prescription [82], following the simultaneous fit to the CRs and

	SR800				SR1100			
	inclusive	ee	$e\mu$	$\mu\mu$	inclusive	ee	$e\mu$	$\mu\mu$
Observed yield	2	0	0	2	1	0	0	1
Total post-fit bkg yield	5.2 ± 1.4	1.8 ± 0.5	2.1 ± 0.8	1.35 ± 0.32	$1.2^{+0.6}_{-0.5}$	$0.51^{+0.22}_{-0.20}$	$0.44^{+0.39}_{-0.33}$	0.22 ± 0.13
Post-fit single-top yield	2.0 ± 1.3	0.6 ± 0.4	1.1 ± 0.7	0.32 ± 0.20	0.32 ± 0.29	0.11 ± 0.10	0.21 ± 0.19	–
Post-fit Z+jets yield	1.40 ± 0.33	0.80 ± 0.24	0.01 ± 0.01	0.59 ± 0.14	0.47 ± 0.15	0.28 ± 0.10	–	0.19 ± 0.11
Post-fit $t\bar{t}$ yield	1.0 ± 0.5	0.27 ± 0.14	0.54 ± 0.25	0.21 ± 0.10	$0.21^{+0.55}_{-0.21}$	$0.06^{+0.16}_{-0.06}$	$0.13^{+0.34}_{-0.13}$	$0.01^{+0.03}_{-0.01}$
Post-fit diboson yield	0.64 ± 0.23	0.14 ± 0.05	0.31 ± 0.12	0.19 ± 0.08	0.13 ± 0.05	0.06 ± 0.03	0.07 ± 0.03	0.01 ± 0.01
Post-fit $t\bar{t} + V$ yield	0.12 ± 0.03	0.01 ± 0.01	0.07 ± 0.02	0.04 ± 0.02	0.03 ± 0.01	–	0.01 ± 0.01	0.01 ± 0.01
Post-fit W+jets yield	0.03 ± 0.03	–	0.04 ± 0.04	–	$0.01^{+0.02}_{-0.01}$	–	$0.01^{+0.02}_{-0.01}$	–
Total MC bkg yield	4.9 ± 1.2	1.7 ± 0.4	2.0 ± 0.7	1.23 ± 0.28	$1.1^{+0.6}_{-0.5}$	$0.46^{+0.21}_{-0.19}$	$0.43^{+0.40}_{-0.33}$	0.18 ± 0.10
MC single-top yield	1.9 ± 1.0	0.57 ± 0.34	1.0 ± 0.6	0.29 ± 0.17	0.29 ± 0.25	0.10 ± 0.08	0.19 ± 0.17	–
MC Z+jets yield	1.15 ± 0.21	0.65 ± 0.17	0.01 ± 0.01	0.48 ± 0.09	0.38 ± 0.10	0.23 ± 0.07	–	0.15 ± 0.09
MC $t\bar{t}$ yield	1.1 ± 0.5	0.29 ± 0.14	0.57 ± 0.26	0.22 ± 0.10	$0.22^{+0.57}_{-0.22}$	$0.07^{+0.18}_{-0.07}$	$0.14^{+0.36}_{-0.14}$	$0.01^{+0.03}_{-0.01}$
MC diboson yield	0.64 ± 0.23	0.14 ± 0.05	0.31 ± 0.12	0.19 ± 0.08	0.13 ± 0.05	0.06 ± 0.03	0.07 ± 0.03	0.01 ± 0.01
MC $t\bar{t} + V$ yield	0.12 ± 0.03	0.01 ± 0.01	0.07 ± 0.02	0.04 ± 0.02	0.03 ± 0.01	–	0.01 ± 0.01	0.01 ± 0.01
MC W+jets yield	0.03 ± 0.03	–	0.04 ± 0.04	–	$0.01^{+0.02}_{-0.01}$	–	$0.01^{+0.02}_{-0.01}$	–
$N_{\mathrm{BSM}}^{\mathrm{limit}}$ exp (95% CL)	$6.4^{+3.0}_{-1.9}$	$4.1^{+1.8}_{-1.1}$	$4.0^{+2.2}_{-0.9}$	$3.9^{+1.6}_{-0.7}$	$3.9^{+2.4}_{-0.5}$	$3.0^{+1.3}_{-0.0}$	$3.0^{+1.3}_{-0.0}$	$3.1^{+0.6}_{-0.1}$
$N_{\mathrm{BSM}}^{\mathrm{limit}}$ obs (95% CL)	4.0	3.0	3.0	4.8	3.9	3.0	3.1	4.1
$\sigma_{\mathrm{BSM}}^{\mathrm{vis}}$[fb]	0.11	0.08	0.08	0.13	0.11	0.08	0.08	0.11

Table 3: The observed and expected background yields in SR800 and SR1100. Both the pre-fit MC expectation and post-fit yields are shown, with each broken down into single-top, Z+jets, $t\bar{t}$, diboson, $t\bar{t} + V$ and W+jets background processes. Model-independent expected and observed limits are set at a 95% CL on the number of events ($N_{\mathrm{BSM}}^{\mathrm{limit}}$) and on the visible cross section ($\sigma_{\mathrm{BSM}}^{\mathrm{vis}}$) of a generic BSM process. Results are shown in each flavor channel and inclusively. The background estimates and their uncertainties are derived from a background-only fit configuration.

a target SR [76]. The signal contribution in both the SR and CRs is accounted for in the fit, though is negligible in the latter. Exclusion fits are performed separately for various branching ratio assumptions, sampling values of $Br(\tilde{t} \to be)$, $Br(\tilde{t} \to b\mu)$, and $Br(\tilde{t} \to b\tau)$, whose sum is unity, in steps of 5%, and reweighting events in the signal samples according to the generated decays. For both SR800 and SR1100, limits are derived in the ee, $e\mu$, $\mu\mu$, and inclusive channels. Observed limits are reported for the SR and channel combination with the lowest expected CL$_S$ value, and therefore best expected sensitivity, at a given mass point and branching ratio. The inclusive channel typically has the largest expected sensitivity when $Br(\tilde{t} \to be)$ and $Br(\tilde{t} \to b\mu)$ are both above 15%, while the ee ($\mu\mu$) channel is more sensitive when $Br(\tilde{t} \to b\mu)$ ($Br(\tilde{t} \to be)$) is below 15%.

The expected and observed exclusion contours on the branching fraction are shown in Fig. 6 for each simulated $\tilde{t}$ mass. The limits are strongest at low values of $Br(\tilde{t} \to b\tau)$, when the number of expected events with electrons or muons in the final state is largest. Expected limits are slightly stronger for increasing $Br(\tilde{t} \to be)$, reflecting a better efficiency in the trigger and identification efficiency of electrons over muons. Exclusion contours reflecting the highest $\tilde{t}$ mass excluded at a 95% CL for a given point in the branching ratio plane are shown in Fig. 7.
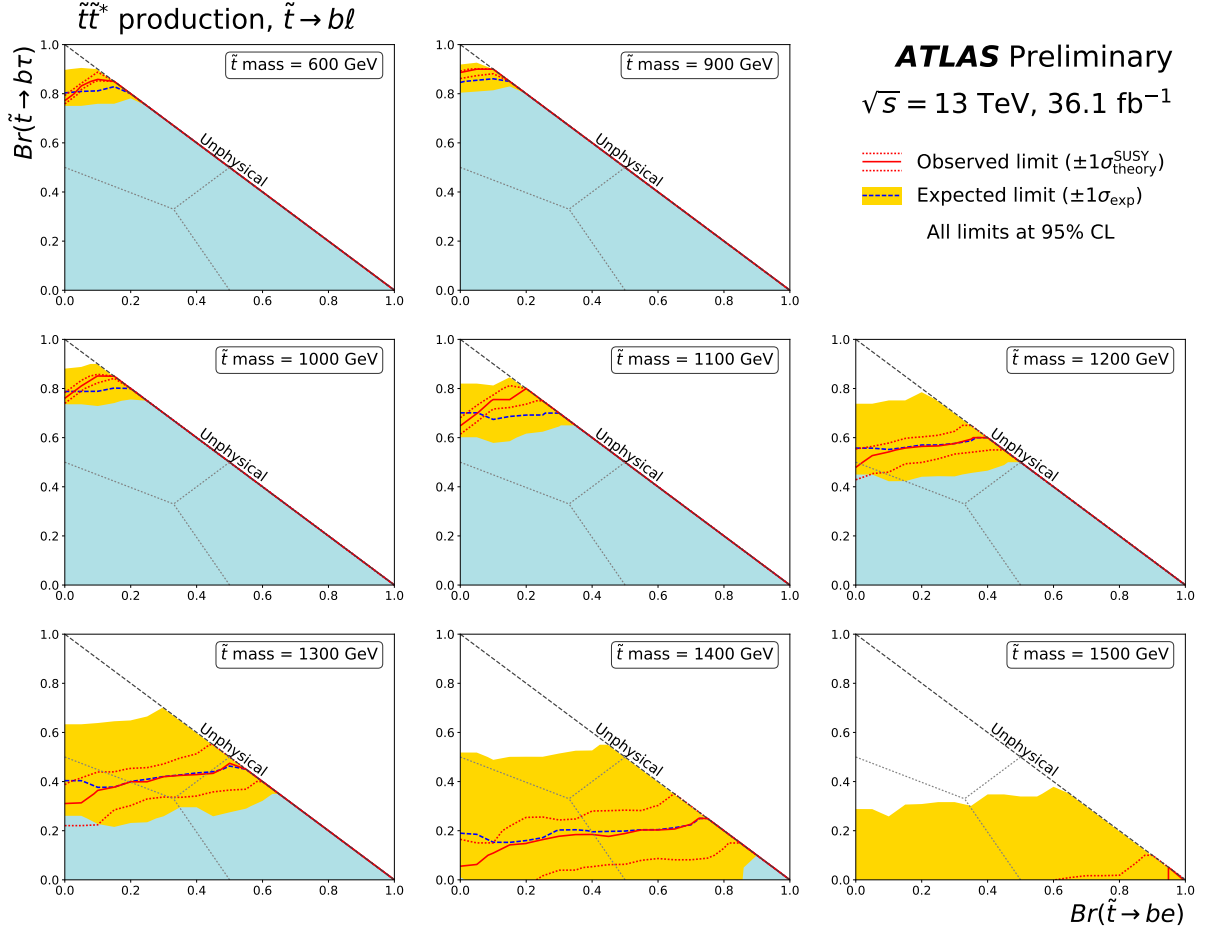
Figure 6: Expected (dashed blue) and observed (solid red) limit curves as a function of $\tilde{t}$ branching ratios for various mass values between 600 and 1500 GeV. The sum of $Br(\tilde{t} \to be)$, $Br(\tilde{t} \to b\tau)$, and $Br(\tilde{t} \to b\mu)$ is assumed to be unity everywhere, and points of equality are marked by a dotted gray line. The shaded blue area under the observed limit curve represents the branching ratios which are excluded at 95% CL. The yellow band reflects the $\pm 1\sigma$ uncertainty on the expected limit due to theoretical, experimental, and MC statistical uncertainties. The dotted red lines correspond to the $\pm 1\sigma$ cross section uncertainty on the observed limit derived by varying the signal cross section by the theoretical uncertainties.
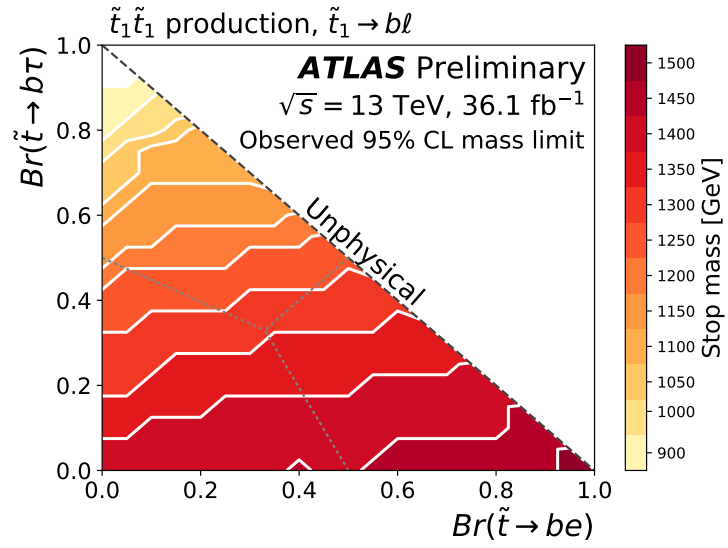
Figure 7: The observed mass limit on the $\tilde{t}$ at 95% CL as a function of $\tilde{t}$ branching ratios. The sum of $Br(\tilde{t} \to be)$, $Br(\tilde{t} \to b\tau)$, and $Br(\tilde{t} \to b\mu)$ is assumed to be unity everywhere, and points of equality are marked by a dotted gray line. This limit is obtained using the nominal $\tilde{t}$ cross section prediction. The mass limit shown corresponds to the highest-mass sample which is excluded. As the branching ratio $Br(\tilde{t} \to b\tau)$ increases, the number of expected events with electrons or muons in the final state decreases, reducing the mass reach of the exclusion.

9 Conclusions

This document presents a search for the pair production of scalar tops, each decaying via an R-parity-violating coupling to a b-quark and a lepton. The final state requires two jets, at least one of which is b-tagged, and two light leptons (electron or muon). The search uses 36.1 fb^{-1}of $\sqrt{s}$ = 13 TeV proton-proton collision data collected with the ATLAS detector at the LHC in 2015 and 2016. No significant excess of events over the Standard Model prediction is observed, and limits are set on the mass of the $\tilde{t}$ at a 95% confidence level. A scan of various $\tilde{t}$ branching ratios is performed to set branching ratio-dependent limits on e, μ, and τ decays. Limits are set on $\tilde{t}$ masses between 600 GeV for large τ decay branching ratios to 1.5 TeV for an e branching ratio of 100%.

References

[1] Y. A. Golfand and E. P. Likhtman,
     Extension of the Algebra of Poincare Group Generators and Violation of p Invariance,
     JETP Lett. **13** (1971) 323.

[2] D. V. Volkov and V. P. Akulov, *Is the Neutrino a Goldstone Particle?* Phys. Lett. B **46** (1973) 109.

[3] J. Wess and B. Zumino, *Supergauge Transformations in Four-Dimensions*,
     Nucl. Phys. B **70** (1974) 39.

[4] J. Wess and B. Zumino, *Supergauge Invariant Extension of Quantum Electrodynamics*,
     Nucl. Phys. B **78** (1974) 1.

[5] S. Ferrara and B. Zumino, *Supergauge Invariant Yang-Mills Theories*,
     Nucl. Phys. B **79** (1974) 413.

[6] A. Salam and J. A. Strathdee, *Supersymmetry and Nonabelian Gauges*,
     Phys. Lett. B **51** (1974) 353.

[7] G. R. Farrar and P. Fayet, *Phenomenology of the Production, Decay, and Detection of New
     Hadronic States Associated with Supersymmetry*, Phys. Lett. B **76** (1978) 575.

[8] J. R. Ellis, J. S. Hagelin, D. V. Nanopoulos, K. A. Olive, and M. Srednicki,
     Supersymmetric Relics from the Big Bang, Nucl. Phys. B **238** (1984) 453.

[9] M. Pospelov, *Particle physics catalysis of thermal Big Bang Nucleosynthesis*,
     Phys. Rev. Lett. **98** (2007) 231301, arXiv: `hep-ph/0605215`.

[10] H. K. Dreiner, *An introduction to explicit R-parity violation*,
     (1997), Adv. Ser. Direct. High Energy Phys. 21, 565 (2010), arXiv: `hep-ph/9707435`.

[11] R. Barbier et al., *R-parity violating supersymmetry*, Phys. Rept. **420** (2005) 1,
     arXiv: `hep-ph/0406039`.

[12] P. Fileviez Perez and S. Spinner, *Supersymmetry at the LHC and the Theory of R-parity*,
     Phys. Lett. B **728** (2014) 489, arXiv: `1308.0524 [hep-ph]`.

[13] P. Fileviez Perez and S. Spinner, *Spontaneous R-Parity breaking and left-right symmetry*,
     Phys. Lett. B **673** (2009) 251, arXiv: `0811.3424 [hep-ph]`.

[14] V. Barger, P. Fileviez Perez, and S. Spinner,
Minimal Gauged U(1)$_{B-L}$ Model with Spontaneous R-Parity Violation,
Phys. Rev. Lett. **102** (2009) 181802, arXiv: `0812.3661 [hep-ph]`.

[15] L. L. Everett, P. Fileviez Perez, and S. Spinner,
The right side of TeV scale spontaneous R-Parity violation, Phys. Rev. D **80** (2009) 055007,
arXiv: `0906.4095 [hep-ph]`.

[16] V. Braun, Y.-H. He, B. A. Ovrut, and T. Pantev, *A heterotic standard model*,
Phys. Lett. B **618** (2005) 252, arXiv: `hep-th/0501070`.

[17] R. Deen, B. A. Ovrut, and A. Purves,
The minimal SUSY B - L model: simultaneous Wilson lines and string thresholds,
JHEP **07** (2016) 043, arXiv: `1604.08588 [hep-ph]`.

[18] R. Barbieri and G. Giudice, *Upper Bounds on Supersymmetric Particle Masses*,
Nucl. Phys. B **306** (1988) 63.

[19] B. de Carlos and J. A. Casas, *One loop analysis of the electroweak breaking in supersymmetric models and the fine tuning problem*, Phys. Lett. B **309** (1993) 320, arXiv: `hep-ph/9303291`.

[20] Z. Marshall, B. A. Ovrut, A. Purves, and S. Spinner,
LSP squark decays at the LHC and the neutrino mass hierarchy, Phys. Rev. D **90** (2014) 015034,
arXiv: `1402.5434 [hep-th]`.

[21] Z. Marshall, B. A. Ovrut, A. Purves, and S. Spinner,
Spontaneous R-Parity breaking, stop LSP decays and the neutrino mass hierarchy,
Phys. Lett. B **732** (2014) 325, arXiv: `1401.7989 [hep-ph]`.

[22] ATLAS Collaboration,
Search for scalar leptoquarks in pp collisions at $\sqrt{s}$ = 13 TeV with the ATLAS experiment,
New J. Phys. **18** (2016) 093016, arXiv: `1605.06035 [hep-ex]`.

[23] ATLAS Collaboration,
Searches for scalar leptoquarks in pp collisions at $\sqrt{s}$ = 8 TeV with the ATLAS detector,
Eur. Phys. J. C **76** (2016) 5, arXiv: `1508.04735 [hep-ex]`.

[24] CMS Collaboration, *Search for pair production of first and second generation leptoquarks in proton–proton collisions at $\sqrt{s}$ = 8 TeV*, Phys. Rev. D **93** (2016) 032004,
arXiv: `1509.03744 [hep-ex]`.

[25] ATLAS Collaboration, *The ATLAS Experiment at the CERN Large Hadron Collider*,
JINST **3** (2008) S08003.

[26] ATLAS Collaboration, *ATLAS Insertable B-Layer Technical Design Report*, ATLAS-TDR-19,
2010, URL: `https://cds.cern.ch/record/1291633`,
ATLAS Insertable B-Layer Technical Design Report Addendum, ATLAS-TDR-19-ADD-1, 2012,
URL: `https://cds.cern.ch/record/1451888`.

[27] ATLAS Collaboration, *Performance of the ATLAS Trigger System in 2015*, (2016),
arXiv: `1611.09661 [hep-ex]`.

[28] ATLAS Collaboration,
Luminosity determination in pp collisions at $\sqrt{s}$ = 8 TeV using the ATLAS detector at the LHC,
Eur. Phys. J. C **76** (2016) 653, arXiv: `1608.03953 [hep-ex]`.

[29] M. Czakon and A. Mitov,
Top++: A program for the calculation of the top-pair cross-section at hadron colliders,
Comput. Phys. Commun. **185** (2014) 2930, arXiv: 1112.5675 [hep-ph].

[30] N. Kidonakis,
Two-loop soft anomalous dimensions for single top quark associated production with a W- or H-,
Phys. Rev. D **82** (2010) 054018, arXiv: 1005.4451 [hep-ph].

[31] N. Kidonakis, *NNLL resummation for s-channel single top quark production*,
Phys. Rev. D **81** (2010) 054028, arXiv: 1001.5034 [hep-ph].

[32] N. Kidonakis, *Next-to-next-to-leading-order collinear and soft gluon corrections for t-channel single top quark production*, Phys. Rev. D **83** (2011) 091503, arXiv: 1103.2792 [hep-ph].

[33] S. Catani, L. Cieri, G. Ferrera, D. de Florian, and M. Grazzini,
Vector boson production at hadron colliders: a fully exclusive QCD calculation at NNLO,
Phys. Rev. Lett. **103** (2009) 082001, arXiv: 0903.2120 [hep-ph].

[34] C. Borschensky et al.,
Squark and gluino production cross sections in pp collisions at $\sqrt{s}$ = 13, 14, 33 and 100 TeV,
Eur. Phys. J. C **74** (2014) 3174, arXiv: 1407.5066 [hep-ph].

[35] ATLAS Collaboration,
Simulation of top-quark production for the ATLAS experiment at $\sqrt{s}$ = 13 TeV,
ATL-PHYS-PUB-2016-004, 2016, URL: https://cds.cern.ch/record/2120417.

[36] S. Alioli, P. Nason, C. Oleari, and E. Re, *A general framework for implementing NLO calculations in shower Monte Carlo programs: the POWHEG BOX*, JHEP **06** (2010) 043,
arXiv: 1002.2581 [hep-ph].

[37] H.-L. Lai et al., *New parton distributions for collider physics*, Phys. Rev. D **82** (2010) 074024,
arXiv: 1007.2241 [hep-ph].

[38] T. Sjöstrand, S. Mrenna, and P. Z. Skands, *PYTHIA 6.4 physics and manual*, JHEP **05** (2006) 026,
arXiv: hep-ph/0603175.

[39] J. Pumplin et al.,
New generation of parton distributions with uncertainties from global QCD analysis,
JHEP **07** (2002) 012, arXiv: hep-ph/0201195.

[40] P. Z. Skands, *Tuning Monte Carlo generators: The Perugia tunes*, Phys. Rev. D **82** (2010) 074018,
arXiv: 1005.3457 [hep-ph].

[41] R. Corke and T. Sjöstrand, *Improved parton showers at large transverse momenta*,
Eur. Phys. J. C **69** (2010) 1, arXiv: 1003.2384 [hep-ph].

[42] ATLAS Collaboration, *Monte Carlo Generators for the Production of a W or Z/γ^* Boson in Association with Jets at ATLAS in Run 2*, ATL-PHYS-PUB-2016-003, 2016,
URL: https://cds.cern.ch/record/2120133.

[43] T. Gleisberg, S. Hoeche, F. Krauss, M. Schonherr, S. Schumann, et al.,
Event generation with SHERPA 1.1, JHEP **02** (2009) 007, arXiv: 0811.4622 [hep-ph].

[44] T. Gleisberg and S. Hoeche, *Comix, a new matrix element generator*, JHEP **12** (2008) 039,
arXiv: 0808.3674 [hep-ph].

[45] F. Cascioli, P. Maierhofer, and S. Pozzorini, *Scattering amplitudes with Open Loops*,
Phys. Rev. Lett. **108** (2012) 111601, arXiv: 1111.5206 [hep-ph].

[46] S. Schumann and F. Krauss,
A Parton shower algorithm based on Catani-Seymour dipole factorisation, JHEP **03** (2008) 038,
arXiv: 0709.1027 [hep-ph].

[47] S. Hoeche, F. Krauss, M. Schonherr, and F. Siegert,
QCD matrix elements + parton showers: The NLO case, JHEP **04** (2013) 027,
arXiv: 1207.5030 [hep-ph].

[48] R. D. Ball et al., *Parton distributions for the LHC Run II*, JHEP **04** (2015) 040,
arXiv: 1410.8849 [hep-ph].

[49] J. Alwall et al., *The automated computation of tree-level and next-to-leading order differential
cross sections, and their matching to parton shower simulations*, JHEP **07** (2014) 079,
arXiv: 1405.0301 [hep-ph].

[50] T. Sjöstrand, S. Mrenna, and P. Z. Skands, *A brief introduction to PYTHIA 8.1*,
Comput. Phys. Commun. **178** (2008) 852, arXiv: 0710.3820 [hep-ph].

[51] L. Lonnblad and S. Prestel, *Matching Tree-Level Matrix Elements with Interleaved Showers*,
JHEP **03** (2012) 019, arXiv: 1109.4829 [hep-ph].

[52] ATLAS Collaboration, *ATLAS Pythia 8 tunes to 7 TeV data*, ATL-PHYS-PUB-2014-021, 2014,
URL: https://cds.cern.ch/record/1966419.

[53] R. D. Ball et al., *Parton distributions with LHC data*, Nucl. Phys. B **867** (2013) 244,
arXiv: 1207.1303 [hep-ph].

[54] M. Krämer, A. Kulesza, R. van der Leeuw, M. Mangano, S. Padhi, et al.,
Supersymmetry production cross sections in pp collisions at $\sqrt{s}$ = 7 TeV, (2012),
arXiv: 1206.2892 [hep-ph].

[55] W. Beenakker, M. Kramer, T. Plehn, M. Spira, and P. Zerwas, *Stop production at hadron colliders*,
Nucl. Phys. B **515** (1998) 3, arXiv: hep-ph/9710451.

[56] W. Beenakker, S. Brensing, M. Kramer, A. Kulesza, E. Laenen, et al.,
Supersymmetric top and bottom squark production at hadron colliders, JHEP **1008** (2010) 098,
arXiv: 1006.4771 [hep-ph].

[57] W. Beenakker, S. Brensing, M. Kramer, A. Kulesza, E. Laenen, et al.,
Squark and Gluino Hadroproduction, Int. J. Mod. Phys. A **26** (2011) 2637,
arXiv: 1105.1110 [hep-ph].

[58] D. J. Lange, *The EvtGen particle decay simulation package*,
Nucl. Instrum. Meth. A **462** (2001) 152.

[59] ATLAS Collaboration, *The ATLAS Simulation Infrastructure*, Eur. Phys. J. C **70** (2010) 823,
arXiv: 1005.4568 [hep-ex].

[60] S. Agostinelli et al., *GEANT4: A simulation toolkit*, Nucl. Instrum. Meth. A **506** (2003) 250.

[61] ATLAS Collaboration, *Summary of ATLAS Pythia 8 tunes*, ATL-PHYS-PUB-2012-003, 2012,
URL: https://cds.cern.ch/record/1474107.

[62] A. D. Martin, W. J. Stirling, R. S. Thorne, and G. Watt, *Parton distributions for the LHC*,
Eur. Phys. J. **C63** (2009) 189, arXiv: 0901.0002 [hep-ph].

[63] P. Laycock et al., "ATLAS Data Preparation in Run 2," ATL-DAPR-PROC-2017-001,
CERN, 2017, URL: https://cds.cern.ch/record/2253427.

[64] ATLAS Collaboration, *Electron and photon energy calibration with the ATLAS detector using data collected in 2015 at $\sqrt{s}$ = 13 TeV*, ATL-PHYS-PUB-2016-015, 2016, URL: https://cds.cern.ch/record/2203514.

[65] ATLAS Collaboration, *Electron efficiency measurements with the ATLAS detector using the 2015 LHC proton–proton collision data*, ATLAS-CONF-2016-024, 2016, URL: https://cds.cern.ch/record/2157687.

[66] ATLAS Collaboration, *Muon reconstruction performance of the ATLAS detector in proton–proton collision data at $\sqrt{s}$ = 13 TeV*, Eur. Phys. J. C **76** (2016) 292, arXiv: 1603.05598 [hep-ex].

[67] M. Cacciari, G. P. Salam, and G. Soyez, *The anti-k_t jet clustering algorithm*, JHEP **04** (2008) 063, arXiv: 0802.1189 [hep-ph].

[68] M. Cacciari, G. P. Salam, and G. Soyez, *FastJet user manual*, Eur. Phys. J. C **72** (2012) 1896, arXiv: 1111.6097 [hep-ph].

[69] ATLAS Collaboration, *Topological cell clustering in the ATLAS calorimeters and its performance in LHC Run 1*, (2016), arXiv: 1603.02934 [hep-ex].

[70] ATLAS Collaboration, *Performance of pile-up mitigation techniques for jets in pp collisions at $\sqrt{s}$ = 8 TeV using the ATLAS detector*, Eur. Phys. J. C **76** (2016) 581, arXiv: 1510.03823 [hep-ex].

[71] M. Cacciari and G. P. Salam, *Pileup subtraction using jet areas*, Phys. Lett. B **659** (2008) 119, arXiv: 0707.1378 [hep-ph].

[72] ATLAS Collaboration, *Jet energy scale measurements and their systematic uncertainties in proton-proton collisions at $\sqrt{s}$ = 13 TeV with the ATLAS detector*, (2017), arXiv: 1703.09665 [hep-ex].

[73] ATLAS Collaboration, *Selection of jets produced in 13 TeV proton–proton collisions with the ATLAS detector*, ATLAS-CONF-2015-029, 2015, URL: https://cds.cern.ch/record/2037702.

[74] ATLAS Collaboration, *Performance of b-Jet Identification in the ATLAS Experiment*, JINST **11** (2016) P04008, arXiv: 1512.01094 [hep-ex].

[75] ATLAS Collaboration, *Optimisation of the ATLAS b-tagging performance for the 2016 LHC Run*, ATL-PHYS-PUB-2016-012, 2016, URL: https://cds.cern.ch/record/2160731.

[76] M. Baak et al., *HistFitter software framework for statistical data analysis*, Eur. Phys. J. C **75** (2015) 153, arXiv: 1410.1280 [hep-ex].

[77] D. R. Tovey, *On measuring the masses of pair-produced semi-invisibly decaying particles at hadron colliders*, JHEP **04** (2008) 034, arXiv: 0802.2879 [hep-ph].

[78] ATLAS Collaboration, *Jet energy resolution in proton–proton collisions at $\sqrt{s}$ = 7 TeV recorded in 2010 with the ATLAS detector*, Eur. Phys. J. C **73** (2013) 2306, arXiv: 1210.6210 [hep-ex].

[79] G. Marchesini et al., *HERWIG: A Monte Carlo event generator for simulating hadron emission reactions with interfering gluons. Version 5.1 - April 1991*, Comput. Phys. Commun. **67** (1992) 465.

[80] S. Gieseke, C. Rohr, and A. Siodmok, *Colour reconnections in Herwig++*, Eur. Phys. J. **C72** (2012) 2225, arXiv: 1206.0041 [hep-ph].

[81] ATLAS Collaboration, *Multi-boson simulation for* 13 *TeV ATLAS analyses*,
      ATL-PHYS-PUB-2016-002, 2016, URL: https://cds.cern.ch/record/2119986.

[82] A. L. Read, *Presentation of search results: The CL(s) technique*, J. Phys. G **28** (2002) 2693.